

1 **Parameter-free resolution estimation based on decorrelation analysis**

2 A. Descloux¹, K.S. Größmayer¹, A. Radenovic¹

3 Affiliations

4 ¹*École Polytechnique Fédérale de Lausanne, Laboratory of Nanoscale Biology, 1015 Lausanne,*
5 *Switzerland*

6

7 Corresponding Authors

8 A. Descloux, email : adrien.descloux@epfl.ch, A. Radenovic, email : aleksandra.radenovic@epfl.ch

9

10 ***Abstract***

11 **Super-resolution microscopy opened diverse novel research directions by overcoming the classical**
12 **resolution limit. Revealing structures beyond the diffraction limit was made possible by exploiting the**
13 **fluorescent emission of individual fluorophores. Involving sample properties to apply these techniques**
14 **entails a redefinition of the resolution parameter. Here, we propose a new method for assessing the**
15 **resolution of individual super-resolved images based on image partial phase auto-correlation. The**
16 **novel algorithm is model-free and does not require any user-defined parameters. We demonstrate its**
17 **performance on a wide variety of imaging modalities, including diffraction-limited techniques. Finally,**
18 **we show how our method can be used to optimize image acquisition and post-processing in super-**
19 **resolution microscopy.**

20

21 **Introduction**

22 Over the past decades, the field of microscopy was enriched with a broad range of novel imaging
23 methods, providing unprecedented insights into sub-cellular structures^{1,2}. When designing a microscopy
24 experiment, one has to select an appropriate imaging modality taking into account the required spatial
25 and temporal resolution. The image quality greatly varies among different techniques and is influenced
26 by sample properties. Image formation for all microscopy techniques (coherent or incoherent,
27 diffraction-limited or super-resolution imaging) can be modelled as the convolution of a ground-truth
28 object with the specific point-spread function plus various method-related noise contributions. In Fourier
29 space, the object spectrum is multiplied by the transfer function of the system. The shape of the transfer
30 function depends on the imaging method employed, but common to all techniques is image low-pass
31 filtering, characterized by a cut-off frequency. This spatial frequency limit already known to Abbe³ is
32 generally expressed as $k_c = NA \frac{2\pi}{\lambda}$, where NA is the sine of the maximum collection angle multiplied by
33 the refractive index and λ the illumination central wavelength, and corresponds to the resolution in
34 coherent imaging.

35 Super-resolution techniques overcome the diffraction limit by exploiting specific fluorophore
36 properties such as stimulated emission or temporal fluctuations. Therefore, image resolution needs to
37 be reconsidered by taking into account the fluorescent properties of the sample to establish a novel
38 resolution measure for super-resolved imaging⁴. Ideally, this resolution criterion should work on a single
39 image, be independent of the imaging method, have no user-dependent settings and be compatible with
40 classical resolution. Such an estimator of resolution is of particular interest for autonomous adaptive
41 microscopes^{5,6} that require robust tools to automatically achieve and maintain optimal performance in
42 long-term imaging of biological samples.

43 In 1982, van Heel⁷ and Saxton⁸ independently proposed the use of Fourier Ring Correlation (FRC)
44 using two independent images of the same object for resolution estimation of electron microscopy
45 images. The concept was quickly expanded to 3D via Fourier Shell Correlation by Harauz⁹ and several
46 threshold concepts have been proposed (0.5 , 0.143^{10} , $2\sigma^{8,11}$, $SSNR^{12}$) to extract a resolution measure.
47 Later, Banterle¹³ and Nieuwenhuizen¹⁴ independently extended, reconsidered and applied the method
48 to assess the resolution of single-molecule localization microscopy (SMLM) images. Similar to electron
49 microscopy, their method requires two stochastically-independent images of the same object and
50 estimates the resolution by computing cross-correlations of Fourier space rings. The cut-off frequency is
51 defined as the spatial frequency where the so-called FRC curve drops below a fixed value equal to 0.143 .

52 In SMLM, the two image realizations are typically accomplished by splitting the image series, i.e.
53 the localizations, into two distinct subsets. In general, it can be achieved for any imaging technique¹⁵ by
54 acquiring two consecutive images under the same conditions. However, maintaining these conditions
55 may be difficult due to, for example, bleaching or temporal fluctuations of the fluorescence signal. This
56 is especially pertinent in live-cell imaging and significantly challenges the stationarity assumption of FRC.

57 Here, we propose a new method able to estimate the resolution based merely on an individual
58 image without any further requirement or a priori knowledge. The algorithm expects only a non-
59 saturated, bandwidth-limited signal with adequate spatial sampling. This novel estimator is based on
60 partial phase correlation and does not rely on any user-defined parameters. The algorithm is fast, uses
61 only linear operations and enables the real-time objective assessment of image resolution and Signal to
62 Noise Ratio (SNR). We successfully applied our new approach on a variety of microscopy data sets,
63 ranging from widefield imaging to SMLM and STED microscopy. We show that our estimator can also be
64 used to optimize image resolution, both during experiments and throughout data post-processing.

65

66 **Method**

67 **Decorrelation analysis**

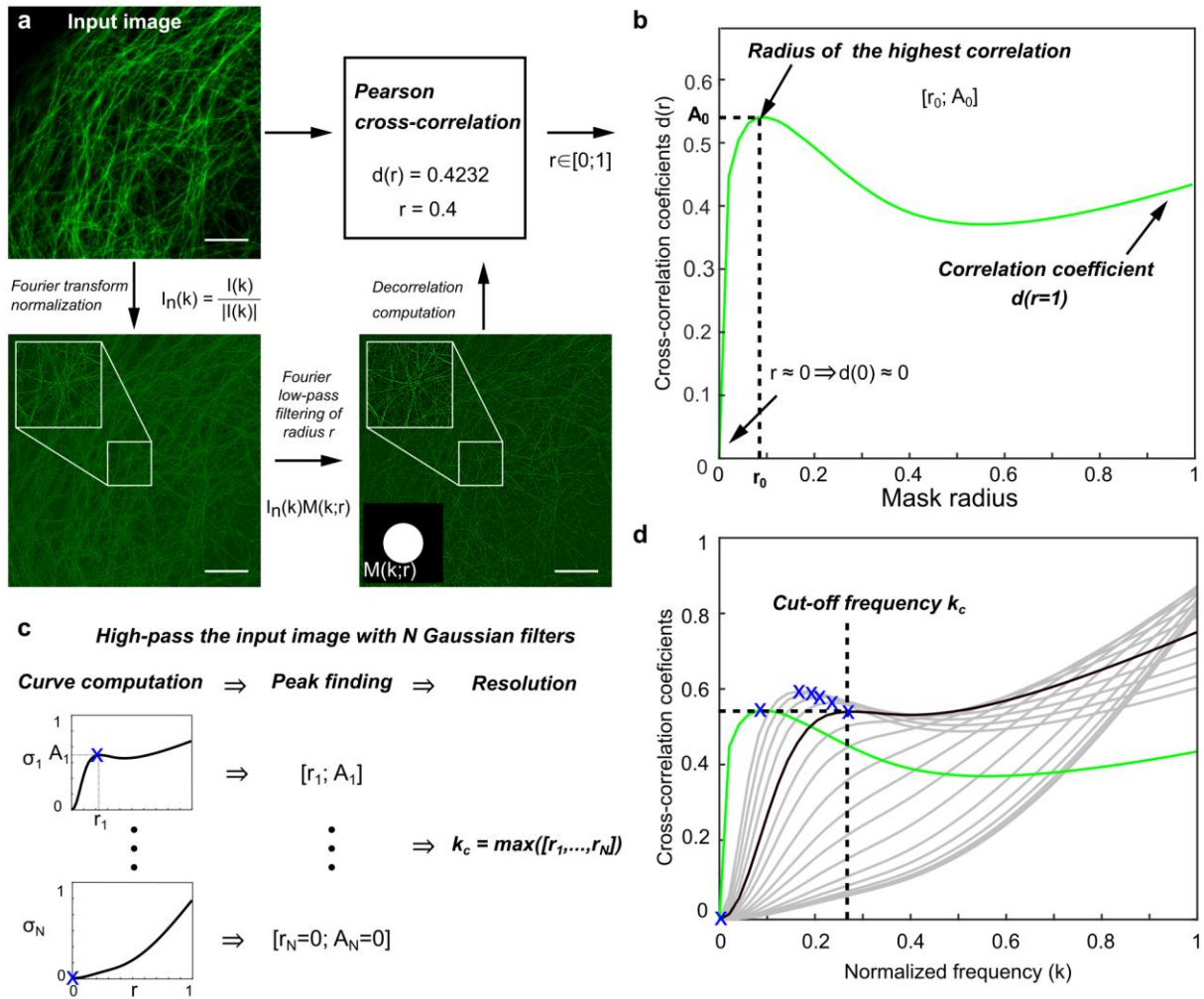
68 To achieve objective threshold-free resolution estimation, we introduce a processing method
69 termed decorrelation analysis. The main algorithm is divided into two steps. First, the Fourier transform
70 of the image is computed after a standard edge apodization to suppress high-frequency artefacts. The
71 Fourier transform is normalized as $I_n(\mathbf{k}) = \frac{I(\mathbf{k})}{|I(\mathbf{k})|}$. The input image $I(\mathbf{k})$ and its normalized version $I_n(\mathbf{k})$
72 are then cross-correlated in Fourier space using Pearson correlation and condensed in a single value
73 between 0 and 1 (Fig. 1a). Second, the operation is repeated, but the normalized Fourier transform is
74 additionally filtered by a binary circular mask of radius $r \in [0,1]$ expressed in normalized frequencies
75 (Fig. 1b). By repeating the calculation, we compute $d(r)$ which is expressed as

$$d(r) = \frac{\iint \text{Re}\{I(\mathbf{k})I_n^*(\mathbf{k})M(\mathbf{k}; r)\} dk_x dk_y}{\sqrt{\iint |I(\mathbf{k})|^2 dk_x dk_y \iint |I_n(\mathbf{k})M(\mathbf{k}; r)|^2 dk_x dk_y}}, \quad (1)$$

76 where $\mathbf{k} = [k_x, k_y]$ denotes Fourier space coordinates, $I(\mathbf{k})$ the Fourier transform of the input image,
77 $I_n(\mathbf{k})$ the normalized Fourier transform and $M(\mathbf{k}; r)$ the binary mask of radius r . \iint is the double integral
78 over k_x and k_y . For a detailed mathematical derivation and additional considerations, see
79 Supplementary Material Section 1.

80 The core idea of the method is that by normalizing the Fourier transform of the input image, we balance
81 the signal and noise contributions while the information of the object structure is preserved in the phase
82 (the phase is responsible for organizing the constructive and destructive interferences of the complex
83 exponentials to form the image, the amplitude plays only a minor role in this process). Taking a radius of
84 the binary mask equal to 1 allows the extraction of the correlation value related to the original ratio of
85 signal and noise. If we consider an image containing only white noise, we see that $d(r = 1) \approx 1$, since

86 the white noise power spectrum is constant by definition (the normalization does not affect the signal).
 87 If we add a bandwidth-limited signal to the image, the correlation value for $r = 1$ will decrease (the
 88 normalization now has a direct effect on the added signal and thus $I_n(\mathbf{k})$ only partially correlates with
 89 $I(\mathbf{k})$.
 90 By decreasing the radius of the mask ($r < 1$), we progressively remove the noise contribution but
 91 preserve the signal due to its bandwidth-limited nature. If the image contains only noise, the cross-



92

93 **Figure 1:** Image decorrelation analysis workflow. (a) Cross-correlation of the image with its Fourier-filtered normalized version.
 94 (b) Cross-correlation coefficient as a function of the mask radius. (c) High-pass filtering of the input image and resolution
 95 estimation. (d) The plot of all decorrelation functions computed for the image and resolution estimation; Green: Decorrelation
 96 function without any high-pass filtering, Grey: Decorrelation functions with high-pass filtering, Blue cross : Local maxima, Black:
 97 decorrelation function of highest frequency peak, Vertical dashed line: cut-off frequency k_c . Scale bar, 5 μm .

98 correlation value will decrease linearly as a function of radius r . If we now add a signal, the decorrelation
99 function $d(r)$ will exhibit a local maximum of amplitude A_0 that indicates the spatial frequency r_0 of best
100 noise rejection and signal preservation ratio. Restricting the mask further removes more signal than
101 noise, therefore reducing the correlation below A_0 until it drops to 0 for $r = 0$. The position r_0 of the
102 local maximum is therefore directly related to the spatial frequency distribution of the image and its
103 amplitude A_0 is positively correlated with the image Signal-to-Noise Ratio (see Supplementary Fig. S1 for
104 detailed plots of decorrelation function behaviour with respect to different noise statistics, aberrated
105 transfer functions, various cut-off frequencies, various SNRs and high-pass filtering strength). For a
106 detailed description of the algorithm, see Supplementary Material Section 1.1.

107 While being related to the spatial frequency content of the image, the position of the maximum
108 does not directly indicate the resolution of the image. The input image is then subjected to a total of N_g
109 high-pass filters (spanning the range from weak to very strong filtering) in order to attenuate the energy
110 of the low frequencies. For each filtered image, a decorrelation function is computed and the peak
111 position r_i and amplitude A_i are extracted, generating a set of $[r_i, A_i]$ pairs (Fig. 1c). If the high-pass
112 filtering removes too much signal, the decorrelation function will not exhibit a local maximum and the
113 peak position and amplitude will both be set to 0. We investigated two different strategies for the
114 resolution estimation: selecting the highest frequency peak or selecting the peak corresponding to the
115 highest geometric mean ($GM = \sqrt{r_i A_i}$) (giving the same weight to the position and amplitude). After
116 processing several simulations and microscopy images taken from different imaging modalities including
117 Confocal, STED, SIM, SOFI and PAINT, we observed that in all cases but confocal images, both criteria
118 provide identical estimates of resolution (see Supplementary Material Section 1.2). We consequently
119 define the resolution estimate as

$$k_c = \max[r_0, \dots, r_{N_g}] \quad (2)$$

120 which corresponds to the local maximum of highest frequency (Fig. 1d). The resolution is then
121 $resolution = \frac{2 * pixel\ size}{k_c}$, where k_c is expressed in normalized frequencies. By computing the resolution
122 with a varying sampling of $d(r)$ and a varying number of high-pass filtering N_g , we confirm the
123 robustness of the algorithm and estimate the precision of the algorithm to be about ± 1 to 3nm,
124 independently of the type of image (see Supplementary Material Fig. S2). We confirmed, via simulations
125 of point emitters, MTFs, rings and crossing lines, that our resolution estimate depends linearly on the
126 frequency support of the image (see Supplementary Material Section 2.1, 2.2 and 2.3) and that the
127 amplitude of the local maximum A_0 before any filtering is directly correlated with the image SNR.

128 Instead of searching for the frequency at which the transfer function vanishes (which can only
129 be measured in the absence of noise), we estimate the highest frequency from the local maxima of the
130 decorrelation functions, enabling parameter-free image resolution estimation. The presented method
131 does not estimate the theoretical resolution as stated by Abbe, but rather the highest frequency with
132 high enough signal with respect to the noise. It provides a rapid and objective way to quantify the
133 frequency content of a single image without any user-defined parameter.

134 **Results**

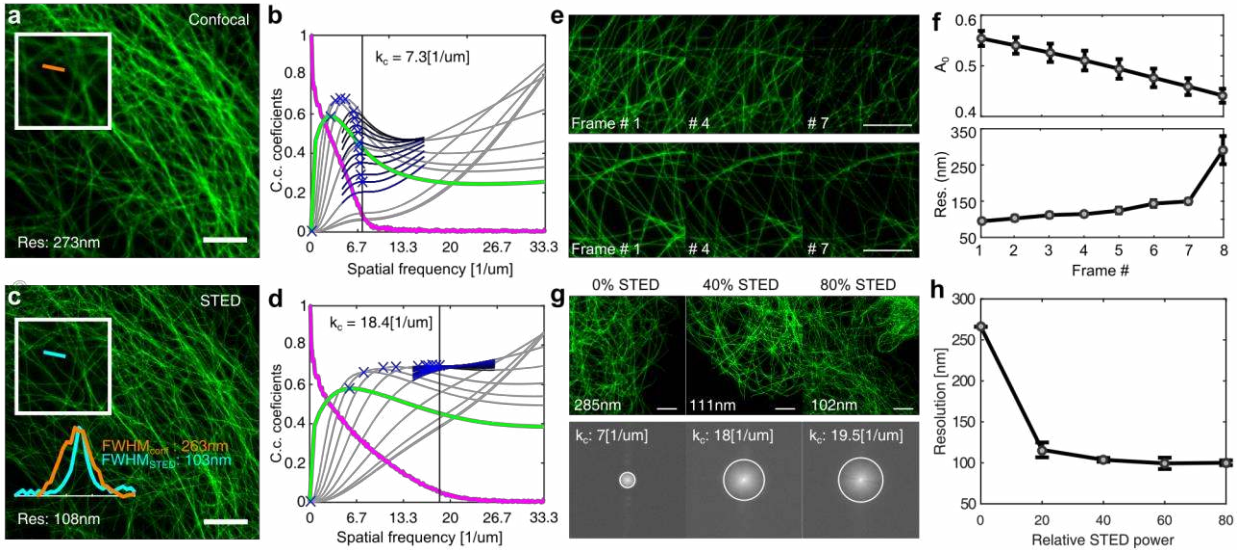
135 To demonstrate the validity and broad applicability of the method, we processed nanorulers data
136 provided by GATTAquant (courtesy of P. Tinnefeld and J. Schmied). DNA origami nanorulers emerged as
137 a platform for reliable performance evaluation across different super-resolution modalities. Their
138 adaptability is due to the fact that one can design these self-assembled nanostructures by placing a
139 defined number of fluorescent dye molecules in precise geometries¹⁶. The resolutions estimated by our
140 algorithm are smaller than the mark-to-mark distances of the nanorulers, which corroborates the fact
141 that they are resolved in all imaging modalities (see Supplementary Material Section 3). After establishing
142 the legitimacy of our method on the DNA origami samples, we extended our analysis to various

143 diffraction-limited (see Supplementary Material Section 4 for bright-field imaging) and super-resolution
144 microscopy images of biological structures, presented in the following. By imaging a z-stack of fluorescent
145 beads, we validated that our resolution estimate fits the expected resolution well. Our estimator
146 provides a unique tool to assess the alignment of an optical setup or the performance of a microscope
147 objective lens using a single experimental image (see Supplementary Material Section 5). All the
148 presented results have been processed using custom Matlab code (source code publicly available at
149 <https://github.com/Ades91/ImDecorr.git>). For ease of use, the algorithm has also been implemented in
150 Java and is available as an open source ImageJ¹⁷ plugin (see Supplementary Material Section 6).

151 **Confocal/STED**

152 We started with confocal¹⁸ and Stimulated Emission Depletion (STED) microscopy^{19,20}, both
153 point-scanning techniques that can be realized on the same setup thus allowing the transition from
154 diffraction-limited to super-resolution imaging. STED microscopy is a super-resolution method that uses
155 confocal illumination to excite the fluorophore and a donut-shaped depletion beam to de-excite (via
156 stimulated emission) most of the surrounding fluorophores prior to fluorescence emission. The
157 resolution of STED microscopy for a given fluorophore is dependent on the spatial and temporal co-
158 alignment of the two beams²¹, the shape, and the quality of the depletion beam and its power²².

159 Using a commercial STED microscope (Leica TCS SP8 3D STED), typically available in state-of-the-
160 art imaging facilities, we imaged the microtubule network of COS-7 cells immuno-labelled with Abberior
161 Star635P, both in confocal and STED mode (pulsed fluorescence excitation at 635nm and pulsed STED
162 depletion laser at 775nm). Fig. 2a-d show the resulting images and their corresponding decorrelation
163 analysis. Throughout the manuscript, we used the following convention: the green line and the grey lines
164 are the original decorrelation functions prior to high-pass filtering and post-high-pass filtering; the blue
165 to black lines are the decorrelation functions with refined mask radius and high-pass filtering range; the



166
 167 **Figure 2: Confocal and STED.** All images show microtubules in fixed COS-7 cells immunolabeled with Abberior Star 635P. (a)
 168 Confocal image and (b) its corresponding decorrelation analysis. Green line: decorrelation functions before high-pass filtering.
 169 Magenta line: Radial average of log of absolute value of Fourier transform of (a). Gray lines: all high-pass filtered decorrelation
 170 functions. Blue to Black lines: decorrelation functions with refined mask radius and high-pass filtering range. Blue crosses: all
 171 local maxima. Dashed vertical line : cut-off k_c (for the sake of readability, we used the same color and style representation for
 172 all the subsequent analysis). (c) STED image of the same structure as in (a) with line profile of selected microtubule and (d) its
 173 corresponding decorrelation analysis. (e) Sequential STED imaging of two different cells (f) SNR estimator and resolution (average
 174 and standard deviation) of a total of 4 STED sequences as a function of time. (g) STED images as a function of STED power. The
 175 lower panel shows the corresponding Fourier space with indicated cut-off frequency. (h) Resolution as a function of STED power
 176 (average and standard deviation of 5 images per STED power). Scale bar, 5 μm . Image acquisition and sample details are
 177 provided in Table S1.

178 blue crosses indicate all the local maxima; the magenta line is the normalized radial-averaged log of the
 179 absolute value of image Fourier transform. The image resolution is indicated as a black vertical line. As
 180 expected, all the decorrelation functions exhibit a local maximum, with STED showing a 2.52-fold
 181 resolution improvement over confocal imaging. We plotted in Fig. 2c the manually selected line profile
 182 of a microtubule cross-section, a method typically used to estimate the resolution. The measured
 183 FWHMs are in good agreement with our estimates.

184 Fig. 2e and f show the result of the analysis performed on a time series of eight consecutive STED
 185 images (each STED image is the average of 8 scans; acquisition time per STED image of 15 sec) and a total
 186 of four sequences (only two shown here). As expected, repeated imaging of the same structure gradually
 187 bleaches the fluorophores, progressively degrading the SNR as indicated by the parameter A_0 . We also
 188 observe a consistent deterioration of the resolution until the 7th frame, where we reach a resolution

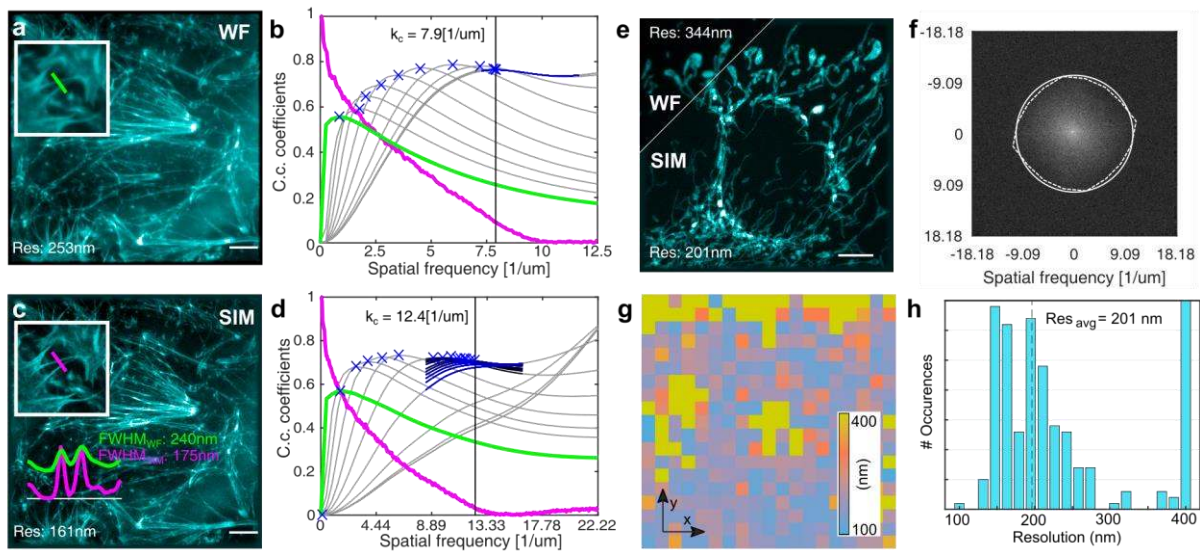
189 close to the one observed in the confocal image. The bleaching is so strong that the structure is no longer
190 continuous. The proposed method confirms the expected degradation of image resolution and provides
191 a quantitative estimation of the image SNR and resolution. Fig. 2g and h illustrate how our resolution
192 estimation can be used to optimize STED imaging. Imaging under several STED illumination powers was
193 performed, always adjusting the excitation power to maintain the optimal dynamic range of the image
194 to avoid noise-limitation of STED resolution¹⁵ (for a total of 5 images per STED power, pixel size 40 nm).
195 We see that using 20% of STED laser power has a significant improvement on the resolution (about 2.4
196 fold) but doubling the power only decreases the resolution by a factor of 1.1 as expected due to the non-
197 linear behaviour of STED. Further increases in STED power do not lead to significant changes in
198 resolution, possibly due to a misalignment of the excitation and STED beam, imperfect “zero” of the STED
199 doughnut as well as excess photo-bleaching and background induced by the STED beam²⁰. We conducted
200 additional experiments, investigating further acquisition parameters such as the STED delay, pixel size
201 and comparing the performance of different dyes to choose the optimal label (see Supplementary
202 Material Section 7). STED microscopy critically depends on photophysics that can also be exploited to
203 increase the resolution (lifetime²¹, photostability²³, spectra²⁴, etc.). For pulsed STED experiments, the
204 best resolution is reached when the depletion pulses immediately follow the excitation pulse. We used
205 our resolution estimate as a readout to adjust the delay between the pulses in the Leica system. Figure
206 S14c shows a drastic improvement in resolution at about $\Delta t=1800\text{ps}$. Previously, an indirect strategy
207 based on minimizing the remaining fluorescence intensity²⁵ or an FRC resolution estimate was used¹⁵.
208 Our algorithm provides a direct and straightforward estimation of image resolution that can be used to
209 objectively find the best acquisition settings and optimize sample preparation, including choice of dye,
210 based on a single image of the sample of interest without imposing additional requirements on the data
211 acquisition scheme. In principle, it should as well be possible to use our resolution estimate to tune the
212 microscope alignment, e.g. to adjust the overlap of STED donut with confocal excitation spot.

213 **WF/SIM**

214 STED has also been used for high-resolution live-cell imaging, but care should be taken to avoid
215 sample damage due to high-depletion laser powers by special imaging procedures²⁰. A super-resolution
216 method that is widely used for imaging dynamics of living cells is Structured Illumination Microscopy^{26–28}
217 (SIM). SIM aims at improving the lateral and axial resolution by multiple imaging of the sample with high-
218 frequency illumination patterns²⁹. The theoretical resolution improvement of SIM is linked to the
219 frequency of the illumination. In practice, SIM resolution depends on the pattern modulation contrast,
220 refractive index mismatch and local distortion of the pattern³⁰. Fig. 3a shows the analysis of a pseudo
221 widefield image, obtained by averaging the raw SIM sequence of actin filaments in U2OS cells³¹ labelled
222 with Phalloidin-Atto488 (obtained on a Delta-Vision|OMX v4, courtesy of T. Huser). A resolution of about
223 253 nm is estimated by decorrelation analysis (cut-off of $7.9[1/\mu\text{m}]$, the pixel size of 80 nm; Fig. 3b). Fig.
224 3c shows the SIM reconstruction (see Supplementary Material Section 8 for the details of the
225 reconstruction) of Fig. 3a and its corresponding decorrelation analysis (cut-off of $12.4[1/\mu\text{m}]$, the pixel
226 size of 45.8 nm; Fig. 3d). We measure a resolution improvement of about 1.56. Measuring the position
227 of the illumination peaks in the Fourier transform of the raw data (4.75 and $9.5[1/\mu\text{m}]$ for the first and
228 second diffraction order respectively), provides a way to estimate the theoretically expected resolution
229 improvement. We observe that the contribution of the first diffraction order with the wide-field
230 resolution $\left(\frac{7.9+4.75}{7.9} \approx 1.6\right)$ fits well with our estimation, indicating that the information encoded in the
231 second diffraction order is not sufficiently contrasted. The use of more advanced reconstruction
232 algorithms may improve this result.

233 So far, we only considered the global resolution, i.e. averaged over the whole image and in all
234 directions. In order to account for non-isotropic resolution, we subdivide the Fourier space in sectors and
235 compute the cut-off frequency as a function of the direction. This is referred to as sectorial resolution

236 (see Supplementary Material Section 9). Fig. 3e shows a different pseudo widefield and SIM
 237 reconstruction of the mitochondria network³¹ in U2OS cells (measured on a Zeiss Elyra S1, courtesy of
 238 M. Sauer, resolution gain of 1.73). Fig.3f displays the Fourier transform of the SIM reconstruction,
 239 overlapped with the sectorial resolution (solid white line) and the average resolution (dashed white



240

241 **Figure 3:** Widefield and SIM (a) Pseudo widefield image of the actin network in fixed U2OS cells labeled with phalloidin-Atto 488
 242 (Courtesy of T. Huser). (b) Corresponding decorrelation analysis. (c) SIM reconstruction of (a) with selected cross-sections. (d)
 243 Corresponding decorrelation analysis. (e) Pseudo widefield and SIM reconstruction of mitochondria network in U2OS cells labeled
 244 with mitotracker (Courtesy of M. Sauer). (f) Sectorial resolution estimation (dashed white line) and average resolution (solid
 245 white circle). (g) Local resolution estimate of (e). (h) Histogram of local resolution shown in (g). Scale bar, 5 μ m. Image acquisition
 246 and sample details are provided in Table S1.

247 circle). Finally, by subdividing the image into smaller tiles (as was done for FRC in¹⁴) (70x70 pixels with an
 248 overlap of 20 pixels), we can estimate the resolution over the whole field-of-view and reveal local
 249 variations in resolution (Fig. 3g). Due to the very weak signal in the top and center part of Fig.3e,
 250 corresponding sub-regions have very large resolution values. In order to preserve the dynamic range, all
 251 resolutions larger than 400nm were set to 400nm. Furthermore, the resolution map can be plotted as a
 252 histogram of resolutions (Fig. 3h), providing another perspective of the image. We also see that the
 253 average resolution is approximately the median of all local resolutions.

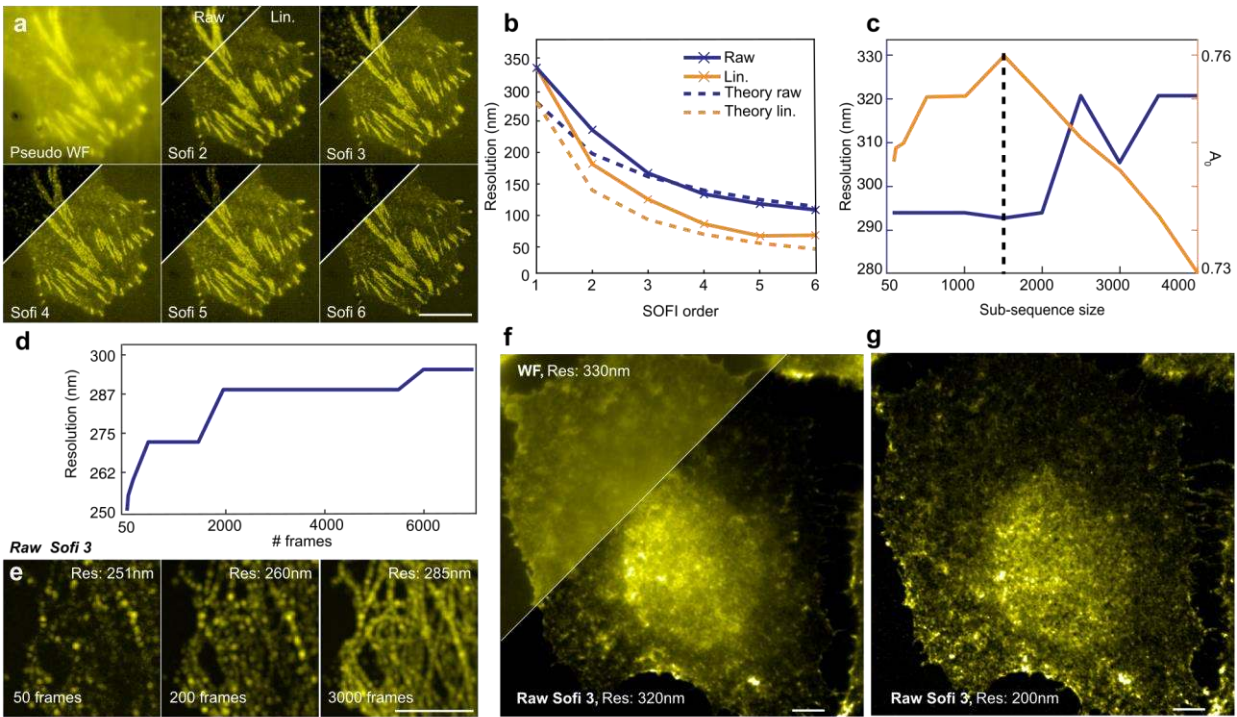
254 **SOFI/Deconvolution**

255 Sub-diffraction imaging can also be achieved by analysing a time series of stochastically blinking
256 emitters. Stochastic Optical Fluctuation Imaging^{32,33} (SOFI) achieves super-resolution by computing high-
257 order spatiotemporal cumulants. SOFI processing is of interest to analyse because it predicts a resolution
258 improvement of $1/\sqrt{n}$, where n is the correlation order and $1/n$ after deconvolution and brightness
259 linearization. It provides an ideal test case for our resolution estimator.

260 Fig. 4a shows the results of SOFI analysis (up to 6th order) of MEF cells expressing paxillin labelled
261 with mEos234 (courtesy of H. Deschout). Fig. 4b displays the results of the decorrelation analysis, where
262 the raw cumulants follow the theoretical resolution improvement up to 70 nm for 6th order linearized
263 SOFI, indicating good blinking statistics. The deviation observed for the widefield (average of the whole
264 sequence, here denoted as SOFI 1) and 2nd order SOFI can be attributed to sub-optimal out-of-focus
265 light rejection. Similarly, the linearized SOFI cumulants, obtained by 10 iterations of Lucy-Ridcharson
266 deconvolution and taking the n th root of the SOFI image, follow a similar trend close to the theoretical
267 value. The deconvolution operation by itself constitutes an interesting case study for our algorithm. We
268 show (see Supplementary Material Section 10) that the resolution can be set to any value, as a function
269 of the input point-spread function and number of iterations of the deconvolution. It is the duty of the
270 user to ensure that the resolution is not enhanced beyond the limit supported by the microscopy
271 method. Our algorithm can thus be used to quantify deconvolution strength but not the validity of the
272 deconvolution.

273 To minimize bleaching and drift artefacts, practical SOFI processing is achieved by first
274 subdividing the whole acquisition into sub-sequences, computing SOFI and averaging the results of the
275 sub-sequences^{35,36}. By using our decorrelation analysis over the resulting SOFI image for various sub-
276 sequences lengths, we are able to identify the optimal resolution-SNR sub-sequence length for the given
277 input data. Fig. 4c shows the results of such an analysis (sub-sequence length ranging from 50 to 4000

278



279

280 **Figure 4:** SOFI (a) Raw SOFI and Linearized SOFI images of focal adhesions in MEF cells expressing paxillin-mEos2 (courtesy of H.
 281 Deschout) shown up to order 6. (b) Estimated and theoretical resolution vs the SOFI order. (c-e) Cumulant analysis of microtubules
 282 in HeLa cells immunolabeled with Alexa Fluor 647. (c) Resolution and SNR estimate vs the sub-sequence size used for SOFI
 283 processing. (d) Resolution estimate vs number of frames. (e) Raw SOFI 3 images for 50, 200 and 3000 frames. (f) Un-optimized
 284 raw SOFI image of fixed HeLa cells labeled with wheat germ agglutinin-Atto 565 using “default” processing parameters. (g) Same
 285 images as (f) after optimization of the resolution. Scale bar, 5 μm. Image acquisition and sample details are provided in Table S1.

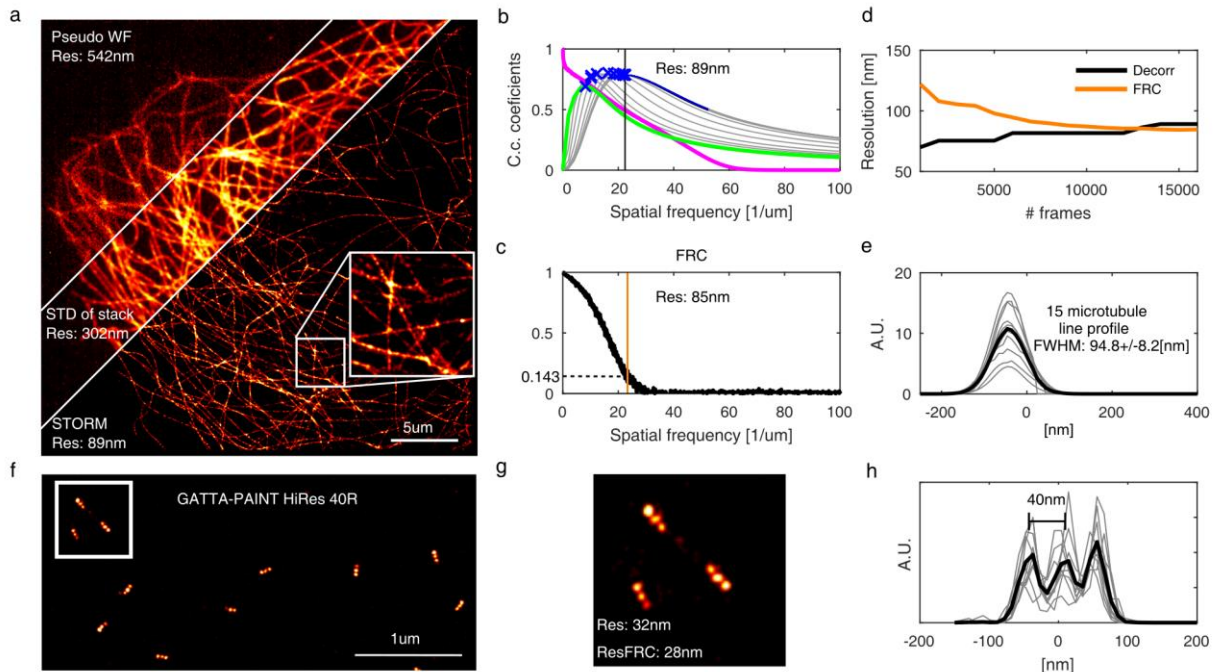
286 frames), performed on a sequence of blinking Alexa647 targeting microtubules of HeLa cell (images
 287 shown in Supplementary Material Section 8, Fig. S6a, 8000 frames in total). For this data, we found an
 288 optimal sub-sequence length of 1500 frames.

289 Fig. 4d and 4e demonstrate how the total number of frames used to compute SOFI impacts the
 290 resolution in HeLa-cell microtubules labelled with Alexa 647. We see that 50 frames already allow the
 291 computation of a 3rd order SOFI image. However, due to the blinking kinetics, many more frames are
 292 required to properly resolve the underlying structure. We also see that the resolution is slightly better
 293 when the image consists only of sparse point-like structures. This is due to the fact that our algorithm
 294 estimates the resolution from a single image. Using only 50 frames, the algorithm sees a sparse
 295 distribution of high-frequency dots. As we include more frames in the analysis, a larger-scale structure

296 containing more low frequencies starts to emerge, leading to a slightly modified resolution estimate.
297 Finally, Fig. 4f shows a raw 3rd order SOFI image of HeLa cells stained with wheat germ agglutinin-Alexa
298 488, processed with default parameters (first 1000 frames removed and sub-sequence length of 500
299 frames). Fig. 4g shows the same image, after optimization of the sub-sequence length and the number
300 of frames to be removed at the beginning and the end of the acquired data to obtain the best resolution
301 (1800 first frames removed, subsequence length of 1000, no frames removed at the end of the
302 sequence). The optimized processing procedure results in a 1.6-fold improvement of resolution
303 compared to the starting image.

304 **Localization microscopy**

305 Finally, we applied our method on Single Molecule Localization Microscopy³⁷⁻³⁹ (SMLM) data. In this case,
306 super-resolution is achieved by the individual localization of a subset of sparsely and stochastically
307 blinking emitters in successive image frames. By fitting the emission point-spread functions, single- and
308 multiple-emitter positions can be determined with nanometric accuracy^{40,41}. To estimate the resolution,
309 our method requires a rendered image. This is typically realized by replacing a filtered set of localization
310 events by a 2D Gaussian of standard deviation equal to the localization uncertainty. The filtering step
311 consists of rejecting unphysical or poor localization events. We validated, using simulations, that our
312 algorithm is also able to correctly estimate the resolution of a localization-based image (see
313 Supplementary Material, Section 11 and Fig. S17). Fig. 5a shows a STORM image of immuno-labelled
314 microtubules (Abberior Flip 565, 16000 frames, localized using single-emitter least square fitting in
315 ThunderSTORM⁴² with default parameters). Each localization was rendered (in Matlab, the pixel size of
316 10 nm) as a normalized Gaussian with standard deviation equal to the localization uncertainty.



317
318
319
320
321
322
323
324

Figure 5: Localization microscopy (a) Pseudo widefield, standard deviation and STORM image of microtubules in COS 7 cells labelled with Abberior Flip 565. (b) Decorrelation analysis of (a). (c) Fourier Ring Correlation analysis of (a). (d) Decorrelation resolution (black line) and FRC resolution (orange line) as a function of a number of frames. (e) Line profile of 15 randomly selected microtubule cross-sections (f) (f) GATTAquant PAINT image of HiRes 40R nanoruler with mark-to-mark distances of 40nm. (g) Zoom of (f) and decorrelation and FRC resolution estimate. (h) 10 line profiles of HiRes 40R molecules indicating a resolution better than 40nm. Image acquisition and sample details are provided in Table S1.

325 With self-blinking dyes^{43,44}, it is not possible to take a widefield image. We thus obtained a pseudo
326 widefield (WF) and standard deviation (STD) image by computing the temporal average and standard
327 deviation of all the frames. We estimate a resolution of 542nm for the pseudo widefield, due to the low
328 SNR of the image and a resolution of 302nm for the STD image. Finally, we estimate a resolution of 89nm
329 for the STORM image. Fig. 5b and c display the corresponding decorrelation resolution estimate and FRC
330 curve, respectively (obtained by splitting the localizations in two odd and even localization subsets to
331 generate two independent realizations). Both estimates agree on the resolution, with FRC (estimated
332 resolution of 85nm) being slightly more optimistic, which is consistent with its behaviour observed in
333 simulations and reported recently by Marsh et al⁴⁰.

334 Fig. 5d shows how our method and FRC resolution vary as a function of the number of frames.
335 We observe a drastic difference in the predicted resolution between the two methods only up to 5000

336 frames. This is due to the fact that FRC requires two images instead of one. For a low number of frames,
337 the localization events are too sparse to produce significant correlations, leading to a large resolution
338 estimate. On the other hand, our method only considers a single image, which is constituted of sparse
339 Gaussians with no apparent structure but a very good SNR (since there is no noise in a rendered
340 localization image). This leads to a very optimistic resolution estimate with the localization uncertainty
341 as a lower bound. As we increase the number of frames, the two random subsets of localization events
342 start to correlate and the FRC resolution estimate starts to decrease. Similarly, as we include more
343 localization events, a larger-scale structure (hence containing low spatial frequencies) starts to emerge.
344 Consequently, our resolution estimate increases as the structure is built up. We finally observe that both
345 methods converge at approximately the same speed at around 12000 frames, with FRC estimating a
346 slightly better resolution⁴⁵. Fig 5e shows a total of 15 microtubules cross-sections randomly selected over
347 Fig. 5a. The apparent average microtubule diameter is about 95nm, which is consistent with the
348 resolution estimate and the secondary immunostaining, which increases the apparent microtubule
349 diameter by 10-30nm^{46,47}.

350 Fig. 5f shows a rendered image of GATTAquant HiRes 40R nanorulers⁴⁸ (courtesy of P. Tinnefeld
351 and J. Schmied). Fig. 5g shows a closeup image of three molecules showing that the three point-source
352 spaced by 40nm can be resolved. Our algorithm estimates a resolution of 32nm while FRC estimates a
353 resolution of 28nm, again being slightly more optimistic than our method. Fig. 5h shows a total of 10 line
354 profiles of individual molecules (grey lines) and their average (solid black line).

355 Finally, it has been shown that multiple blinking events can severely impact the FRC resolution
356 estimate by introducing spurious correlations¹⁴. While this effect can in principle be mitigated, it requires
357 an accurate estimation of the underlying blinking statistics⁴⁹. We show (see Supplementary Material Fig.
358 S18) that our resolution estimate is independent on the probability of multiple blinking event, as our
359 method does not require any assumption on the blinking kinetics.

360 ***Discussion***

361 We proposed a new method for parameter-free resolution and SNR estimation of a single
362 microscopy image. We were able to circumvent the need for a threshold by introducing a new form of
363 partial phase correlation. In principle, our method can be applied to any imaging technique, including
364 electron microscopy, atomic force microscopy, X-ray tomography and live-cell imaging. Here, we
365 demonstrated its broad applicability by applying it to various types of microscopy images, ranging from
366 bright field to single-molecule localization microscopy images. By processing nanoruler data, we showed
367 that the method can be used to quantitatively assess the resolution which enabled an optimization of
368 imaging parameters, post-processing and reconstruction of acquired data. Our approach provides a new
369 and objective way to quantify the effective resolution in super-resolution microscopy. The extension of
370 our method to 3D would require a reformulation of our algorithm in the spherical coordinate.

371 By developing an open-source ImageJ plug-in, we enable the use of our method to non-image
372 processing specialist. We provide a unique and novel approach for resolution estimation based on the
373 analysis of a single image that can be used for image processing optimization and image reconstruction
374 comparison. We envision that our new resolution estimate represents a powerful tool for on-the-fly
375 microscopy setup characterization and optimization as well as for automated microscopes. We hope that
376 our method will be adopted by the ever-growing microscopy community as an everyday tool, helping
377 them to achieve high-quality research.

378 **Materials and methods**

379 ***Cell culture***

380 HeLa and COS-7 cells were cultured at 37 °C and 5 % CO₂ using DMEM high glucose with pyruvate (4.5 g
381 l⁻¹ glucose, with GlutaMAX™ supplement) supplemented with 10 % fetal bovine serum and 1 x penicillin-
382 streptomycin (all gibco®, Thermo Fisher Scientific).

383 ***Cell fixation and immunostaining***

384 Cells were seeded in Lab-tek® II chambered cover slides (nunc) or on 18 mm high-precision No. 1.5
385 borosilicate coverslips (Marienfeld) in 12 well plates (Thermo Fisher Scientific) 1-2 days before fixation
386 in DMEM (see cell culture) or DMEM high glucose w/o phenol red (4.5 g l⁻¹ glucose) supplemented with
387 4 mM L-glutamine, 10 % fetal bovine serum and 1x penicillin-streptomycin (all gibco®, Thermo Fisher
388 Scientific).

389 ***HeLa cells:***

390 Cells were washed twice in pre-warmed buffer (microtubule stabilizing buffer (MTSB): 100 mM PIPES pH
391 6.8, 2mM MgCl₂, 5 mM EGTA or PBS for wheat germ agglutinin (WGA) staining), followed by application
392 of pre-warmed fixation buffer (3.7 % paraformaldehyde (PFA), 0.2 % Triton X-100 in MTSB or 3.7 %
393 paraformaldehyde (PFA) in PBS for wheat germ agglutinin (WGA) staining) for 15 min at room
394 temperature (RT). Cells were then washed three times for 5 min each with 1 x PBS and stored in 50 %
395 glycerol in 1 x PBS at 4 °C or the immunostaining protocol was continued to prepare samples for
396 fluorescence imaging. Fixed and permeabilized cells were blocked with 3 % BSA in 1 x PBS and 0.05 %
397 Triton X-100 for 60 min at RT or overnight at 4 °C.

398 Cells fixed without permeabilization were stained with 5 ng ml⁻¹ WGA-Atto 565 for 10min followed by
399 three times 5 min washes with 1 x PBS. The blocked samples with prior permeabilization were
400 immediately incubated with a mix of primary anti-tubulin antibody (1 mg ml⁻¹ DM1a mouse monoclonal
401 (ab80779) 1:150 dilution, Abcam) in antibody incubation buffer for 60 min at RT (AIB: 1 % BSA in 1 x PBS
402 and 0.05 % Triton X-100). Cells were then washed three times for 5 min each with AIB, followed by
403 incubation with donkey anti-mouse-Alexa Fluor 647 antibody (0.005 mg ml⁻¹ Invitrogen) for 60 min at RT.
404 This and all subsequent steps were performed in the dark. All cells were again washed three times for 5

405 min each with AIB and incubated for 15 min post-fixation with 2 % PFA in 1 x PBS followed by three 5 min
406 washes with PBS. Cells were imaged immediately or stored in 50 % glycerol in 1 x PBS at 4 °C until imaging.

407 ***COS-7 cells:***

408 The protocol is similar as described previously by Chazeau et al.⁵⁰. Cells were washed twice in pre-
409 warmed DMEM w/o phenol red (see cell culture) following 90s incubation with extraction buffer
410 (microtubule stabilizing buffer 2 (MTSB2: 80 mM PIPES, 7 mM MgCl₂, 1 mM EGTA, 150mM NaCl, 5mM
411 D-glucose adjust pH to 6.8 using KOH) with freshly added 0.3 % Triton X-100 (AppliChem) and 0.25%
412 glutaraldehyde (stock solution 50% electron microscopy grade, Electron Microscopy Sciences).
413 Immediately afterwards, pre-warmed 4 % paraformaldehyde (PFA) in PBS was incubated for 15 min at
414 room temperature (RT). Cells were then washed three times for 5 min each with 1 x PBS and stored in
415 50 % glycerol in 1 x PBS at 4 °C or the immunostaining protocol was continued. Next, a freshly prepared
416 solution of 10mM NaBH₄ in 1x PBS was incubated on the cells for 7 minutes followed by one quick wash
417 in 1xPBS, and two washes 10min 1xPBS on an orbital shaker. Cells were permeabilized in PBS with 0.25
418 % Triton X-100 for 7min followed by blocking with blocking buffer (BB: 2% (w/v) BSA, 10mM glycine,
419 50mM ammonium chloride NH₄Cl in PBS pH 7.4 for 60 min at RT or overnight at 4 °C.

420 The blocked samples were immediately incubated with primary anti-tubulin antibody (clone B-5-1-2
421 ascites fluid 1:100-1:200 dilution, Sigma-Aldrich) in BB for 60 min at RT. Cells were then washed three
422 times for 5 min each with BB, followed by incubation with either donkey anti-mouse-Alexa Fluor 647
423 antibody for SOFI imaging (donkey anti-mouse (H+L) highly cross-adsorbed at 0.005 mg ml⁻¹ Invitrogen),
424 donkey anti-mouse-AbberiorFlip565 for SMLM imaging (preparation see below at 1:200 dilution) or goat
425 anti-mouse-AbberiorStar635P (at 0.005-0.01 mg ml⁻¹ Abberior), goat anti-mouse-Atto594 (at 0.0025-
426 0.005 mg ml⁻¹ Atto-tec), donkey anti-mouse-Alexa Fluor 594 antibody (donkey anti-mouse (H+L) highly
427 cross-adsorbed at 0.005 mg ml⁻¹ Invitrogen) or donkey anti-mouse-biotin (Biotin-SP (long spacer)

428 AffiniPure Donkey Anti-Mouse IgG (H+L), at 1:200 Jackson ImmunoResearch) for STED imaging for 60 min
429 at RT. This and all subsequent steps were performed in the dark. All cells were again washed three times
430 for 5 min each with AIB and incubated for 15 min post-fixation with 2 % PFA in 1 x PBS followed by three
431 5 min washes with PBS. Cells with biotinylated secondary antibody were additionally incubated with
432 streptavidin-Atto490LS (at 0.01 mg ml⁻¹ Atto-tec) in PBS for 30min followed by 3 washes for 5 min in PBS
433 before post-fixation. Cells were imaged immediately or stored in 50 % glycerol in 1 x PBS at 4 °C until
434 SOFI or SMLM imaging. For STED microscopy, cells were mounted on a coverglass slide (Thermo Fisher
435 Scientific) using Mowiol-DABCO (preparation see below) and allowed to harden for at least 24h at RT.
436 Cells were imaged within 1 week of sample preparation.

437 ***Preparation of labeled proteins***

438 2 mg ml⁻¹ donkey anti-mouse (H+L) highly cross-adsorbed antibody (Invitrogen) was incubated with
439 AbberiorFlip565-NHS (Abberior) and 2 mg ml⁻¹ WGA (Vector Labs) was incubated with Atto565-NHS
440 ester (Atto-tec) at a ratio of 1: 6 for 1h at RT while shaking with the pH raised to 8.3 using sodium
441 bicarbonate. The mixture was purified using illustra NAP Columns (GE Healthcare) according to
442 manufacturer's instructions and eluted with slightly acidic PBS to recover the labeled antibody at neutral
443 pH. The protein concentration was estimated by absorption spectrometry to <1.5 mg ml⁻¹ donkey anti-
444 mouse AbberiorFlip565 and 0.5 mg ml⁻¹ WGA-Atto565.

445 ***Imaging buffer and embedding medium***

446 The samples for SOFI using Alexa Fluor dyes were imaged in a 50 mM Tris-Hcl pH 8.0, 10 mM NaCl
447 buffer containing an enzymatic oxygen scavenging system (2.5 mM protocatechuic acid (PCA) and 50 nM
448 Protocatechuate- 3,4-Dioxygenase from Pseudomonas Sp. (PCD) with >3 Units m g⁻¹) and a thiol (2-
449 Mercaptoethylamine). The thiol and a stock solution of 100 mM PCA in water, pH adjusted to 9.0 with
450 NaOH, were always prepared fresh. PCD was aliquoted at a concentration of 10 µM in storage buffer

451 (100 mM Tris-HCl pH 8.0, 50 % glycerol, 50 mM KCl, 1 mM EDTA) at -20 °C and thawed immediately before
452 use. The samples for SMLM using Abberior Flip 565 were imaged in 1x PBS. Mowiol-DABCO for STED
453 embedding was prepared as described in the manufacturer protocol (Roth Gebrauchsanweisung Mowiol
454 488). Aliquots were kept at -20C and thawed immediately before use.

455 ***Microscope setups***

456 ***Widefield, SOFI and SMLM***

457 Data for Fig. 4e-g, Fig. 5, Fig. S3a-d and Fig. S7a were acquired on a standard widefield custom build
458 microscope. A total of 4 illumination laser lines (405nm 200 mW Roithner; 488nm 200mW Toptica;
459 561nm 350mW Quantum laser; 635nm 1W Roithner) are collimated, expanded and combined with
460 dichroic filters. The beams are then cropped with a rectangular aperture of approx. 7.2 mm placed in the
461 conjugated object plane, resulting in a 120x120 μm field of view. The beams are then focused with an
462 achromatic lens ($f = 200\text{mm}$) and reflected by a 3mm thick Quad Line Beamsplitter (R405/488/561/635;
463 Semrock) in the back focal plane of the objective (Nikon 60x/1.27NA SR water immersion). The
464 fluorescence signal is focused on the camera (Orca Flash 4.0; Hamamatsu) with a 200mm achromatic
465 lens. The sample position is controlled in X and Y by a Scan-plus IM 120x80 (Marzheuser) and in Z by a
466 Nano-Z piezo nanopositioner (Mad City Labs). All acquisitions were performed using Micromanager. The
467 laser intensities used in the experiments can be found in Table S1.

468 ***Confocal and STED***

469 Confocal and STED microscopy was performed at the EPFL bioimaging and optics platform (BIOP) using a
470 Leica SP8 STED 3X. The setup consists in a Leica DMI 8 inverted microscope body equipped with a white
471 light laser (470-670nm) and a Leica HC PL APO 100X/1.40 oil objective for STED. For STED imaging we
472 used the 775nm pulsed depletion laser and detected the fluorescence on HyD detectors. 100% 775nm
473 laser power corresponds to 403mW, 100% 633nm laser power corresponds to 1.12mW, 100% 488nm

474 laser power corresponds to 0.33mW and 100% 520nm laser power corresponds to 0.43mW (power
475 measurements were performed after the objective by the BIOP). The laser powers and other acquisition
476 parameters used in the experiments can be found in Table S1.

477 ***Data processing***

478 The algorithm is implemented in MATLAB (Mathworks) and ImageJ. All the codes are available upon
479 request.

480 ***Acknowledgments***

481 The authors would like to thank Dr. T. Lukes and Prof. T. Laser for insightful discussions. We also thank
482 Dr. H. Deschout, Dr. M. Muller, Prof. T. Huser, Prof. M. Sauer for sharing SOFI and SIM data. We also
483 thank Dr. J. Schmied and Prof. P. Tinnefeld for sharing GATTAquant nanoruler data. This project has been
484 partly funded by the European Union's Horizon 2020 research and innovation program via grant
485 686271/SEFRI 16.0047. K.G. acknowledges the support from the Horizon 2020 Framework Program of
486 the European Union under the Marie Skłodowska-Curie Grant Agreement No. [750528]. A.D. and A.R.
487 acknowledge the support from Zeiss IDEAS center. We would like to thank EPFL BioImaging & Optics Core
488 Facility (EPFL-BIOP) for access to confocal and STED microscopes.

489 ***Author contributions***

490 A.D. proposed and developed the method, processed all the presented data, wrote the Matlab and Java
491 code. K.S.G. prepared all the cells and performed measurements. A.R. supervised the research. A.D.
492 wrote the manuscript with comments of all co-authors at all stages.

493 ***Data and materials availability***

494 All data needed to evaluate the conclusions in the paper are present in the paper and/or the
495 Supplementary Materials. Additional data related to this paper may be requested from the authors.

496 **Bibliography**

- 497 1. Sahl, S. J., Hell, S. W. & Jakobs, S. Fluorescence nanoscopy in cell biology. *Nat. Rev. Mol. Cell Biol.*
498 **18**, 685–701 (2017).
- 499 2. Sigal, Y. M., Zhou, R. & Zhuang, X. Visualizing and discovering cellular structures with super-
500 resolution microscopy. *Science* **361**, 880–887 (2018).
- 501 3. Abbe, E. Beiträge zur Theorie des Mikroskops und der mikroskopischen Wahrnehmung. *Arch. für*
502 *Mikroskopische Anat.* **9**, 413–418 (1873).
- 503 4. Sheppard, C. J. R. Resolution and super-resolution. *Microsc. Res. Tech.* **80**, 590–598 (2017).
- 504 5. Power, R. M. & Huisken, J. Adaptable, illumination patterning light sheet microscopy. *Sci. Rep.* **8**,
505 1–11 (2018).
- 506 6. Štefko, M., Ottino, B., Douglass, K. M. & Manley, S. Autonomous illumination control for
507 localization microscopy. *Opt. Express* **26**, 30882–30900 (2018).
- 508 7. Heel, M. Van. Similarity measures between images. *Ultramicroscopy* **21**, 95–100 (1987).
- 509 8. Saxton, W. & Baumeister, W. The correlation averaging of a regularly arranged bacterial cell
510 envelope protein. *J. Microsc.* **127**, 127–138 (1982).
- 511 9. Harauz, G. & van Heel, M. Exact filters for general geometry three dimensional reconstruction.
512 *Optik* **78**, 146–156 (1986).
- 513 10. Rosenthal, P. B. & Henderson, R. Optimal determination of particle orientation, absolute hand,
514 and contrast loss in single-particle electron cryomicroscopy. *J. Mol. Biol.* **333**, 721–745 (2003).
- 515 11. Orlova, E. V. *et al.* Structure of keyhole limpet hemocyanin type 1 (KLH1) at 15 Å resolution by
516 electron cryomicroscopy and angular reconstitution. *J. Mol. Biol.* **271**, 417–437 (1997).

- 517 12. Unser, M., Trus, B. L. & Steven, A. C. A new resolution criterion based on spectral signal-to-noise
518 ratio. *Ultramicroscopy* **23**, 39–52 (1987).
- 519 13. Banterle, N., Bui, K. H., Lemke, E. A. & Beck, M. Fourier ring correlation as a resolution criterion
520 for super-resolution microscopy. *J. Struct. Biol.* **183**, 363–367 (2013).
- 521 14. Nieuwenhuizen, R. P. J. *et al.* Measuring image resolution in optical nanoscopy. *Nat. Methods*
522 **10**, 557–562 (2013).
- 523 15. Tortarolo, G., Castello, M., Diaspro, A., Koho, S. & Vicidomini, G. Evaluating image resolution in
524 stimulated emission depletion microscopy. *Optica* **5**, 32 (2018).
- 525 16. Raab, M. *et al.* Using DNA origami nanorulers as traceable distance measurement standards and
526 nanoscopic benchmark structures. *Sci. Rep.* **8**, 1780 (2018).
- 527 17. Abramoff, M. D., Magalhães, P. J. & Ram, S. J. Image processing with ImageJ. *Biophotonics Int.*
528 **11**, 36–42 (2004).
- 529 18. Minsky, M. Memoir on inventing the confocal scanning microscope. *Scanning* **10**, 128–138
530 (1988).
- 531 19. Hell, S. W. & Wichmann, J. Breaking the diffraction resolution limit by stimulated emission:
532 stimulated-emission-depletion fluorescence microscopy. *Opt. Lett.* **19**, 780 (1994).
- 533 20. Vicidomini, G., Bianchini, P. & Diaspro, A. STED super-resolved microscopy. *Nat. Methods* **15**,
534 173–182 (2018).
- 535 21. Tortarolo, G., Sun, Y., Teng, W., Ishitsuka, Y. & Vicidomini, G. Photon-separation to enhance the
536 spatial resolution of pulsed STED microscopy. *Nanoscale* **11**, 1754–1761 (2019).
- 537 22. Westphal, V. & Hell, S. W. Nanoscale resolution in the focal plane of an optical microscope.

- 538 *Phys. Rev. Lett.* **94**, 1–4 (2005).
- 539 23. Oracz, J., Westphal, V., Radzewicz, C., Sahl, S. J. & Hell, S. W. Photobleaching in STED nanoscopy
540 and its dependence on the photon flux applied for reversible silencing of the fluorophore. *Sci.*
541 *Rep.* **7**, 11354 (2017).
- 542 24. Vicidomini, G., Moneron, G., Eggeling, C., Rittweger, E. & Hell, S. W. STED with wavelengths
543 closer to the emission maximum. *Opt. Express* **20**, 5225–5236 (2012).
- 544 25. Galiani, S. *et al.* Strategies to maximize the performance of a STED microscope. *Opt. Express* **20**,
545 7362–7374 (2012).
- 546 26. Heintzmann, R. & Cremer, C. G. *Laterally modulated excitation microscopy: improvement of*
547 *resolution by using a diffraction grating.* (International Society for Optics and Photonics, 1999).
- 548 27. Frohn, J. T. Super-resolution fluorescence microscopy by structured light illumination. (ETH
549 Zürich, 2000).
- 550 28. Gustafsson, M. G. L. Surpassing the lateral resolution limit by a factor of two using structured
551 illumination microscopy. *J. Microsc.* **198**, 82–87 (2000).
- 552 29. Heintzmann, R. & Huser, T. Super-Resolution Structured Illumination Microscopy. *Chem. Rev.*
553 **117**, 13890–13908 (2017).
- 554 30. Demmerle, J. *et al.* Strategic and practical guidelines for successful structured illumination
555 microscopy. *Nat. Protoc.* **12**, 988–1010 (2017).
- 556 31. Müller, M., Mönkemöller, V., Hennig, S., Hübner, W. & Huser, T. Open-source image
557 reconstruction of super-resolution structured illumination microscopy data in ImageJ. *Nat.*
558 *Commun.* **7**, 1–6 (2016).

- 559 32. Dertinger, T., Colyer, R., Iyer, G., Weiss, S. & Enderlein, J. Fast, background-free, 3D super-
560 resolution optical fluctuation imaging (SOFI). *Proc. Natl. Acad. Sci. U. S. A.* **106**, 22287–92 (2009).
- 561 33. Dertinger, T., Colyer, R., Vogel, R., Enderlein, J. & Weiss, S. Achieving increased resolution and
562 more pixels with Super-resolution Optical Fluctuation Imaging (SOFI). *Opt. Express* **18**, 18875–
563 18885 (2010).
- 564 34. Deschout, H. *et al.* Complementarity of PALM and SOFI for super-resolution live-cell imaging of
565 focal adhesions. *Nat. Commun.* **7**, 13693 (2016).
- 566 35. Geissbuehler, S. *et al.* Mapping molecular statistics with balanced super-resolution optical
567 fluctuation imaging (bSOFI). *Opt. Nanoscopy* **1**, 4 (2012).
- 568 36. Peeters, Y. *et al.* Correcting for photodestruction in super-resolution optical fluctuation imaging.
569 *Sci. Rep.* **7**, 10470 (2017).
- 570 37. Rust, M. J., Bates, M. & Zhuang, X. W. Sub-diffraction-limit imaging by stochastic optical
571 reconstruction microscopy (STORM). *Nat Methods* **3**, 793–795 (2006).
- 572 38. Betzig, E. *et al.* Imaging intracellular fluorescent proteins at nanometer resolution. *Science* **313**,
573 1642–5 (2006).
- 574 39. Sauer, M. & Heilemann, M. Single-Molecule Localization Microscopy in Eukaryotes. *Chem. Rev.*
575 **117**, 7478–7509 (2017).
- 576 40. Marsh, R. J. *et al.* Artifact-free high-density localization microscopy analysis. *Nat. Methods* **15**,
577 689 (2018).
- 578 41. Legant, W. R. *et al.* High-density three-dimensional localization microscopy across large
579 volumes. *Nat. Methods* **13**, 359–365 (2016).

- 580 42. Ovesny, M., Krizek, P., Borkovec, J., Svindrych, Z. & Hagen, G. M. ThunderSTORM : a
581 comprehensive ImageJ plug-in for PALM and STORM data analysis and super-resolution imaging.
582 *Bioinformatics* **30**, 2389–2390 (2014).
- 583 43. Fölling, J. *et al.* Photochromic Rhodamines Provide Nanoscopy with Optical Sectioning **.
584 *Angew. Chemie - Int. Ed.* **46**, 6266–6270 (2007).
- 585 44. Bossi, M. *et al.* Multicolor Far-Field Fluorescence Nanoscopy through Isolated Detection of
586 Distinct Molecular Species. *Nano Lett.* **8**, 2463–2468 (2008).
- 587 45. Lambert, T. J. & Waters, J. C. Navigating challenges in the application of superresolution
588 microscopy. *J. Cell Biol.* **216**, 53–63 (2016).
- 589 46. Mikhaylova, M. *et al.* Resolving bundled microtubules using anti-tubulin nanobodies. *Nat.*
590 *Commun.* **6**, 1–7 (2015).
- 591 47. Pleiner, T., Bates, M. & Görlich, D. A toolbox of anti – mouse and anti – rabbit IgG secondary
592 nanobodies. *J. Cell Biol.* **217**, 1143–1154 (2017).
- 593 48. Schmied, J. J. *et al.* Fluorescence and super-resolution standards based on DNA origami Flaws in
594 evaluation schemes for pair- input computational predictions. *Nat. Methods* **9**, 1133–1134
595 (2012).
- 596 49. Annibale, P., Vanni, S., Scarselli, M., Rothlisberger, U. & Radenovic, A. Quantitative Photo
597 Activated Localization Microscopy : Unraveling the Effects of Photoblinking. *PLoS One* **6**, e22678
598 (2011).
- 599 50. Chazeau, A., Katrukha, E. A., Hoogenraad, C. C. & Kapitein, L. C. Studying neuronal microtubule
600 organization and microtubule-associated proteins using single molecule localization microscopy.
601 *Methods Cell Biol.* **131**, 127–149 (2016).

